Simultaneous Fidelity and Regularization Learning for Image Restoration

Dongwei Ren, Wangmeng Zuo, David Zhang, Lei Zhang, and Ming-Hsuan Yang

Abstract—Most existing non-blind restoration methods are based on the assumption that a precise degradation model is known. As the degradation process can only partially known or inaccurately modeled, images may not be well restored. Rain streak removal and image deconvolution with inaccurate blur kernels are two representative examples of such tasks. For rain streak removal, although an input image can be decomposed into a scene layer and a rain streak layer, there exists no explicit formulation for modeling rain streaks and the composition with scene layer. For blind deconvolution, as estimation error of blur kernel is usually introduced, the subsequent non-blind deconvolution process does not restore the latent image well. In this paper, we propose a principled algorithm within the maximum a posterior framework to tackle image restoration with a partially known or inaccurate degradation model. Specifically, the residual caused by a partially known or inaccurate degradation model is spatially dependent and complexly distributed. With a training set of degraded and ground-truth image pairs, we parameterize and learn the fidelity term for a degradation model in a task-driven manner. Furthermore, the regularization term can also be learned along with the fidelity term, thereby forming a simultaneous fidelity and regularization learning model. Extensive experimental results demonstrate the effectiveness of the proposed model for image deconvolution with inaccurate blur kernels and rain streak removal. Furthermore, for image restoration with precise degradation process, e.g., Gaussian denoising, the proposed model can be applied to learn the proper fidelity term for optimal performance based on visual perception metrics.

Index Terms—Image restoration, blind deconvolution, rain streak removal, task-driven learning.

1 Introduction

MAGE restoration that aims to recover the latent clean image from a degraded observation is a fundamental problem in low-level vision. However, the degradation generally is irreversible, making image restoration an ill-posed inverse problem. While significant advances have been made in the past decades, it is challenging to develop proper models for various image restoration tasks.

In general, the linear degradation process of a clean image ${\bf x}$ can be modeled as

$$\mathbf{y} = A\mathbf{x} + \mathbf{n},\tag{1}$$

where \mathbf{n} is additive noise, \mathcal{A} is degradation operator, and \mathbf{y} is degraded observation. By changing the settings of the degradation operator and noise type, they can be applied to different image restoration tasks. For example, \mathcal{A} can be an identity matrix for denoising, a blur kernel convolution for deconvolution, and a downsampling operator for super-resolution, to name a few. The maximum a posterior (MAP) model for image restoration can then be formulated as

$$\mathbf{x} = \arg\min_{\mathbf{x}} \frac{\lambda}{2} \|A\mathbf{x} - \mathbf{y}\|_{2}^{2} + \mathcal{R}(\mathbf{x}),$$
 (2)

where λ is a trade-off parameter, $\mathcal{R}(\mathbf{x})$ is the regularization term associated with image prior, and the fidelity term is specified by degradation \mathcal{A} as well as noise \mathbf{n} [1]–[3]. Assuming the noise \mathbf{n}

D. Ren and D. Zhang are with the School of Computer Science and Technology, Harbin Institute of Technology, Harbin 150001, China, and also with the Department of Computing, Hong Kong Polytechnic University, Hong Kong. E-mail: rendongweihit@gmail.com; csdzhang@comp.polyu.edu.hk

W. Zuo is with the School of Computer Science and Technology, Harbin Institute of Technology, Harbin 150001, China. E-mail: cswmzuo@gmail.com L. Zhang is with the Department of Computing, Hong Kong Polytechnic University, Hong Kong. E-mail: cslzhang@comp.polyu.edu.hk

M.-H. Yang is with School of Engineering, University of California, Merced, CA 95344. E-mail: mhyang@ucmerced.edu

is additive white Gaussian, the fidelity term can be characterized by the ℓ_2 -norm.

When the degradation operator A is precisely known, noise and image prior models play two key roles in the MAP-based image restoration model. Two widely-used types of noise distributions are Gaussian and Poisson. Other distributions, e.g., hyper-Laplacian [4], Gaussian Mixture Model (GMM) [5] and Mixture of Exponential Power (MoEP) [6], are also introduced for modeling complex noise. For image prior, gradient-based models, e.g., total variation [7] and hyper-Laplacian distribution [1], are first studied due to simplicity and efficiency. Subsequently, patchbased [2] and non-local similarity [8], [9] models are developed to characterize more complex and internal dependence among image patches. Recently, data-driven and task-driven learning methods have also been exploited to learn regularization from training images. The approach based on fields of experts (FoE) [10] is designed to learn the distribution of filter responses on images. Following the FoE framework, numerous discriminative learning approaches, e.g., cascaded shrinkage field (CSF) [3] and trainable non-linear reaction diffusion (TNRD) [11], [12], use the stagewise learning scheme to enhance the restoration performance as well as computational efficiency.

However, the precise degradation process for most restoration tasks is not known and thus the degradation process is modeled as

$$\mathbf{y} = A\mathbf{x} + q(\mathbf{x}; B) + \mathbf{n}. \tag{3}$$

In the restoration stage, only the model parameter \mathcal{A} is known, while the form $g(\mathbf{x};\cdot)$, the noise type \mathbf{n} or the parameters \mathcal{B} are unknown. Here we define this problem as *image restoration with partially known or inaccurate degradation models*.

Image deconvolution with inaccurate blur kernels and rain streak removal are two representative image restoration tasks with

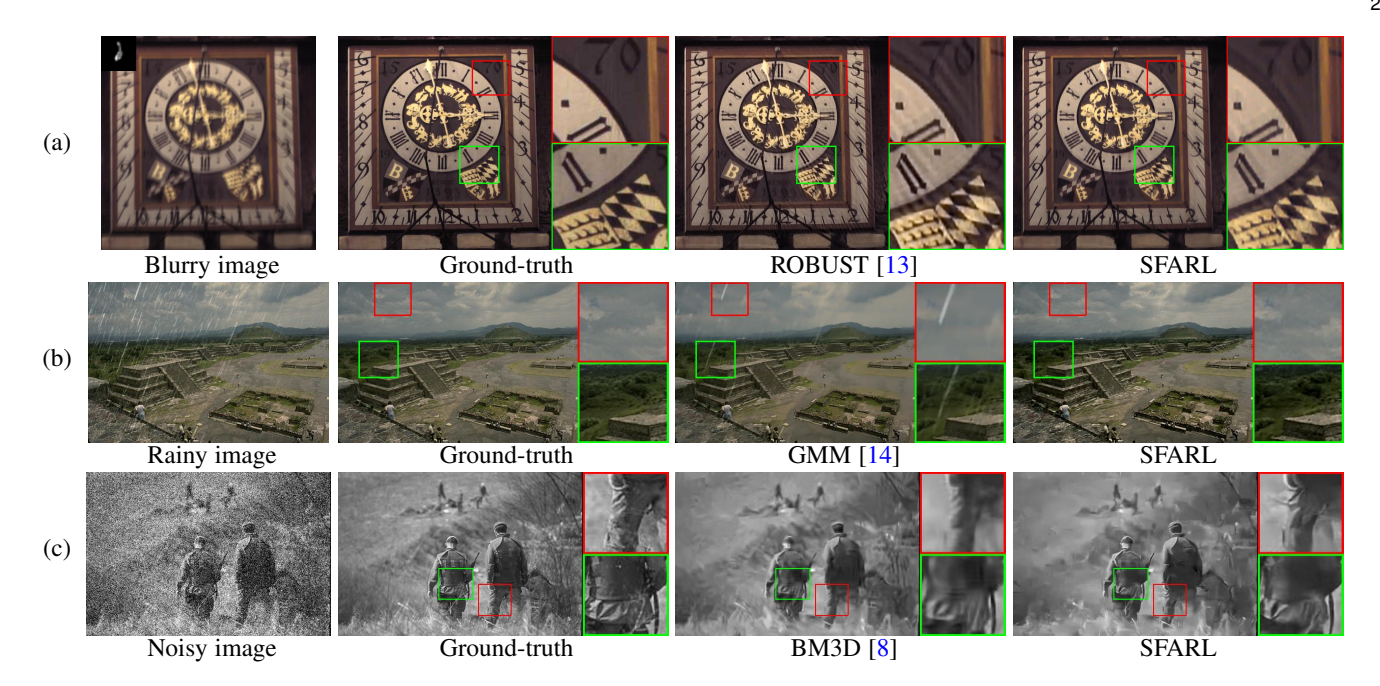


Fig. 1: Illustration of the SFARL model on three restoration tasks. (a) In image deconvolution with inaccurate blur kernels, The SFARL method is effective in relieving the ringing artifacts. (b) For rain streak removal, the SFARL model can produce more clean image than GMM [14]. (c) Even for Gaussian denoising, when the optimization target is negative SSIM, the result by the SFARL algorithm is visually more plausible than that by the BM3D method [8].

partially known or inaccurate degradation models. Image deconvolution with an inaccurate blur kernel is a subproblem of blind deconvolution which generally includes blur kernel estimation and non-blind deconvolution. In the blur kernel estimation stage, the kernel error $\triangle \mathbf{k}$ generally is inevitable to be introduced by a specific method [15]–[20]. In the non-blind deconvolution stage, the degradation model can then be written as

$$\mathbf{y} = \mathbf{k} \otimes \mathbf{x} + \triangle \mathbf{k} \otimes \mathbf{x} + \mathbf{n},\tag{4}$$

where \otimes denotes the 2D convolution operator. Thus, the subproblem in the non-blind deconvolution stage is equivalent to *image deconvolution with inaccurate blur kernels*. Based on (3), we have $g(\mathbf{x}; \Delta \mathbf{k}) = \Delta \mathbf{k} \otimes \mathbf{x}$. Conventional non-blind deconvolution methods are sensitive to kernel error and usually result in ringing and other artifacts [1], [2], as shown in Figure 1.

For rain streak removal, an input mage y can be represented as the composition of a scene image layer x and a rain streak layer x_r . However, it remains challenging to model rain streak with any explicit formulation. On one hand, a linear summation $y = x + x_r$ is usually used for combining the scene image and rain streak layers [14], [21]. On the other hand, it has been suggested [22] that a complex model based on screen blend is more effective for combining the scene image and rain streak layers,

$$\mathbf{y} = \mathbf{x} - \mathbf{x} \cdot \mathbf{x}_r + \mathbf{x}_r,\tag{5}$$

where \cdot denotes the element-wise product. By setting $g(\mathbf{x}; \mathbf{x}_r) = -\mathbf{x} \cdot \mathbf{x}_r$, rain streak removal can be treated as an image restoration problem with a partially known degradation model, i.e., both $g(\mathbf{x}; \mathbf{x}_r)$ and \mathbf{x}_r cannot be explicitly modeled in the deraining stage. As shown in Figure 1, the method [14] is less effective for modeling rainy scenes, resulting in an over-smooth image with visible steaks.

Image restoration with partially known or inaccurate degradation models cannot be simply addressed by noise modeling. From (3), we define the residual image as

$$\mathbf{r} = \mathbf{y} - A\mathbf{x} = g(\mathbf{x}; B) + \mathbf{n}. \tag{6}$$

Due to the introduction of $g(\mathbf{x}; \mathcal{B})$, even \mathbf{n} is white, the residual \mathbf{r} is spatially dependent and complexly distributed. Although several noise models have been suggested for complex noise modeling, these are all based on the independent and identically distributed (i.i.d.) assumption and ineffective for modeling the spatial dependency of the residual. Furthermore, the characteristics of \mathbf{r} is task specific and there exists no universal model that can be applied to all problems, thereby making it more challenging to solve (6).

In this paper, we propose a principled fidelity learning algorithm for image restoration with partially known or inaccurate degradation models. For either kernel error caused by a specific kernel estimation method or rain steaks, the resulting residual r is not entirely random and can be characterized by spatial dependency and distribution models. Thus, a task-driven scheme is developed to learn the fidelity term from a training set of degraded and ground-truth image pairs. For modeling spatial dependence and complex distribution, the residual \mathbf{r} is characterized by a set of nonlinear penalty functions based on filter responses, leading to a parameterized formulation of the fidelity term. Such a fidelity term is effective and flexible in modeling complex residual patterns and spatial dependency caused by partially known or inaccurate degradation for a variety of image restoration tasks. Furthermore, for different tasks (e.g., rain steak removal and image deconvolution with inaccurate blur kernels), the residual patterns are also different. With task-driven learning, the proposed method can adaptively tailor the fidelity term to specific inaccurate or partially known degradation models.

We show the regularization term can be parameterized and learned along with the fidelity term, resulting in our simultaneous fidelity and regularization learning (SFARL) model. In addition, we characterize the regularizer by a set of nonlinear functions on filters responses of clean image. The SFARL model is formulated as a bi-level optimization problem where a gradient descent scheme is used to solve the inner task and stage-wise parameters are learned from the training data. Experimental results on image deconvolution and rain steak removal demonstrate the effectiveness of the SFARL modelin terms of quantitative metrics and visual quality (see Figure 1(a)(b)). Furthermore, for image restoration with precise degradation process, e.g., non-blind Gaussian denoising, the SFARL model can be used to learn the proper fidelity term for optimizing visual perception metrics, and obtain results with better visual quality (see Figure 1(c)).

The contributions of this work are summarized as follows:

- We propose a principled algorithm for image restoration with partially known or inaccurate degradation. Give an image restoration task, our model can adaptively learn the proper fidelity term from the training set for modeling the spatial dependency and highly complex distribution of the task-specific residual caused by partially known or inaccurate degradation.
- We present a bi-level optimization model for simultaneous learning of the fidelity term as well as regularization term, and stage-wise model parameters for task-specific image restoration.
- We carry out experiments on rain streak removal and image deconvolution with inaccurate blur kernels to validate the effectiveness of the SFARL model. We show that the SFARL model can also be applied to image restoration with precise degradation model (e.g., Gaussian denoising) and achieve results with better visual quality and improved perception metrics.

2 RELATED WORK

For specific vision tasks, numerous methods have been proposed for image deconvolution with inaccurate blur kernels and rain steak removal. However, considerably less effort has been made to address image restoration with partially known or inaccurate degradation models. In this section, we review related topics most relevant to this work, including noise modeling, discriminative image restoration, image deconvolution with inaccurate blur kernels, and rain steak removal.

2.1 Noise Modeling

For vision tasks based on robust principal component analysis (RPCA) or low rank matrix factorization (LRMF), noise is often assumed to be sparsely distributed and can be characterized by ℓ_p -norms [4], [23]. However, the noise in real scenarios is usually more complex and cannot be simply modeled using ℓ_p -norms. Consequently, GMM and its variants have been used as universal approximations for modeling complex noise. In RPCA models, Zhao et al. [24] use a GMM model to fit a variety of noise types, such as Gaussian, Laplacian, sparse noise and their combinations. For LRMF method, a GMM model is used to approximate unknown noise, and its effectiveness has been validated in face modeling and structure from motion [5]. In addition, a GMM model is also extended for noise modeling by

low rank tensor factorization [25], and generalized to the Mixture of exponential power (MoEP) scheme [6] for modeling complex noise. To determine the parameters of a GMM model, the Dirichlet process has been suggested to estimate the number of Gaussian components under variational Bayesian framework [26]. Recently, the weighted mixture of ℓ_1 -norm, ℓ_2 -norm [27] and Gaussian [28], [29] models have also been used for blind denoising with unknown noise.

However, noise modeling cannot be readily used to address image restoration with partially known or inaccurate degradation models. The residual **r** caused by inaccurate degradation is not i.i.d. Thus, both spatial dependency and complex noise distribution need to be considered to characterize the residual.

2.2 Discriminative Image Restoration

In a MAP-based image restoration model, the regularization term is associated with a statistical prior and assumed to be learned solely based on clean images in a generative manner, e.g., K-SVD [30], GMM [2], and FoE [10]. Recently, discriminative learning has been extensively studied in image restoration. In general, discriminative image restoration aims to learn a fast inference procedure by optimizing an objective function using a training set of the degraded and ground-truth image pairs. One typical discriminative learning approach is to combine existing image prior models with truncated optimization procedures [31], [32]. For example, the cascade of shrinkage fields (CSF) [3], [33] use truncated half-quadratic optimization to learn stage-wise model parameters of a modified FoE. On the other hand, the trainable nonlinear reaction diffusion (TNRD) model [11], [12] unfolds a fixed number of gradient descent inference steps. Non-parametric methods, such as regression tree fields (RTF) [31], [32] and filter forests [34], are also used for modeling image priors. Recently, Zhang et al. [35] use deep convolutional neural networks (CNNs) to learn priors for image restoration.

Existing discriminative image restoration methods, however, are all based on the precise degradation assumption. These algorithms focus on learning regularization terms in a discriminative framework such that the models can be applied to arbitrary images and blur kernels. In contrast, we propose a discriminative learning algorithm that considers both fidelity and regularization terms, and apply it to image restoration with partially known or inaccurate degradation models.

2.3 Image Deconvolution with Inaccurate Blur Kernels

Typical blind deconvolution approaches consist of two stages: blur kernel estimation and non-blind deconvolution. Existing methods mainly focus on the first stage [16], [17], [20], [36], and considerable attention has been paid to blur kernel estimation. For the second stage, conventional non-blind deconvolution methods usually are used to restore the clean image based on the estimated blur kernels. Despite significant progress has been made in blur kernel estimation, errors are inevitable introduced after the first stage. Furthermore, non-blind deconvolution methods are not robust to kernel errors, and artifacts are likely to be introduced or exacerbated during deconvolution [1], [2].

One intuitive solution is to design specific image priors to suppress artifacts [37]–[40]. To the best of our knowledge, there exists only one attempt [13] to implicitly model kernel error in fidelity term,

$$\mathbf{x} = \arg\min_{\mathbf{x}} \frac{\lambda}{2} \|\mathbf{k} \otimes \mathbf{x} - \mathbf{y} + \mathbf{z}\|^2 + \mathcal{R}(\mathbf{x}) + \tau \|\mathbf{z}\|_1.$$
 (7)

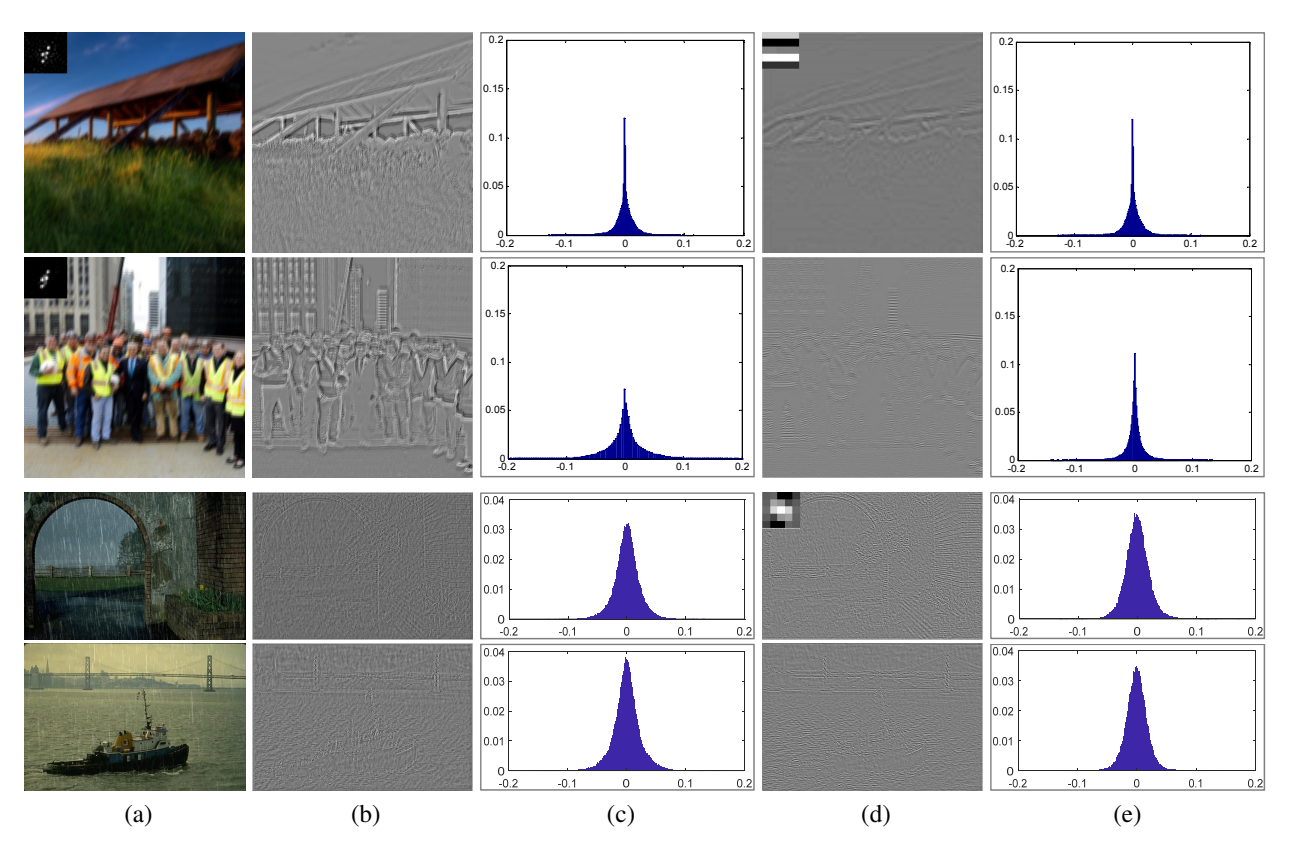


Fig. 2: Examples of residual images in image deconvolution with inaccurate blur kernels and rain streak removal. (a) Blurry images as well as blur kernels estimated by Xu and Jia [16] for deconvolution, and synthetic rainy images. (b) Residual images (from the first stage for deconvolution and from the second stage for rain streak removal) by the SFARL model in which the intensities are magnified for better view. (c) Histograms of residual images in (b), (d) One of the learned filters in fidelity model, and its responses on residual images in (b) in which the responses are also magnified. (e) Histograms of responses in (d).

Here the residual ${\bf r}$ is defined as ${\bf r}={\bf z}+{\bf n}$, where ${\bf z}$ is associated with the ℓ_1 -norm, and ${\bf n}$ is additive white Gaussian noise. However, a method based on ${\bf z}$ with the ℓ_1 -norm does not model the spatial dependency of residual signals. The method [13] alleviates the effect of kernel errors at the expense of potential over-smooth restoration results. In this work, we focus on the second stage of blind deconvolution, and propose the SFARL model to characterize the kernel error of a specific kernel estimation method.

2.4 Rain Streak Removal

Rain streak and scene composition models are two important issues for removing rain drops from input images. Based on the linear model $y = x + x_r$, the MAP-based deraining model can be formulated as

$$\mathbf{x} = \arg\min_{\mathbf{x}} \frac{\lambda}{2} \|\mathbf{y} - \mathbf{x} - \mathbf{x}_r\|^2 + \mathcal{R}(\mathbf{x}) + \mathcal{Q}(\mathbf{x}_r)$$
s.t. $\forall i, \ 0 \le x_i \le y_i, \ 0 \le x_{ri} \le y_i,$

where $Q(\cdot)$ denotes the regularization term of the rain streak layer, and the inequality constraints are introduced to obtain non-negative solutions of \mathbf{x} and \mathbf{x}_r [14].

In [21], hand-crafted regularization is employed to impose smoothness on the image layer and low rank on the rain streak layer. In [14], both image and rain streak layers are modeled as GMMs that are separately trained on clean patches and rain steak patches. Based on the screen blend model, Luo et al. [22] use the discriminative dictionary learning scheme to separate rain

streaks by enforcing that two layers need to share fewest dictionary atoms. Instead of using explicit analytic models, the SFARL method is developed based on a data-driven learning approach to accommodate the complexity and diversity of rain steak and scene composition models.

3 Proposed Algorithm

We consider a class of image restoration problems, where the degradation model is partially known or inaccurate but a training set of degraded and ground-truth image pairs is available. To handle these problems, we use a flexible model to parameterize the fidelity term caused by partially known or inaccurate degradation. For a given problem, a task-driven learning approach can then be developed to obtain a task-specific fidelity model from the training data.

In this section, we first present our method for parameterizing the fidelity term to characterize the spatial dependency and complex distribution of the residual signals. In addition, the regularization term is also parameterized, resulting in our simultaneous fidelity and regularization learning model. Finally, we propose a task-driven manner to learn the proposed model from the training data.

3.1 Fidelity Term

The fidelity term is used to characterize the spatial dependency and highly complex distribution of the residual image $\mathbf{r} = g(\mathbf{x}; \mathcal{B}) + \mathbf{n}$. Figure 2(b) shows two residual examples for image deconvolution

with inaccurate blur kernels and rain streak removal. The histogram of each residual image is also shown in the figure. First, it can be observed that the residual image is significantly different from a Gaussian distribution and is not i.i.d. Second, Figure 2(c) shows that the distributions of pixel values vary significantly for different residual images, which indicate that it is less effective to characterize the residual image ${\bf r}$ in the raw data space.

To model the spatial dependency in \mathbf{r} , we use a set of linear filters $\{\mathbf{p}_i\}_{i=1}^{N_f}$ with diverse patterns to extract information from $g(\mathbf{x};\mathcal{B})$, where N_f is the number of filters. We utilize a set of non-linear penalty functions $\{\mathcal{D}_i\}_{i=1}^{N_f}$ to describe the distribution of filter responses. Therefore, we propose a principled residual modeling in the fidelity term,

$$\mathcal{F}(\mathbf{x}) = \lambda \sum_{j=1}^{N} \sum_{i=1}^{N_f} \mathcal{D}_i \left((\mathbf{p}_i \otimes (\mathcal{A}\mathbf{x} - \mathbf{y}))_j \right), \tag{9}$$

where \mathcal{A} is the degradation operator defined in (1) and \otimes is the 2D convolution operator. In the proposed fidelity term, the parameters include $\Theta_f = \{\lambda, \mathbf{p}_i, \mathcal{D}_i\}_{i=1}^{N_f}$. When $N_f = 1$, \mathbf{p}_1 is delta function and \mathcal{D}_1 is the squared ℓ_2 -norm, the proposed model (9) is equivalent to the standard MAP-based model in (2).

Due to the introduction of linear filters $\{\mathbf{p}_i\}_{i=1}^{N_f}$ and penalty functions $\{\mathcal{D}_i\}_{i=1}^{N_f}$, the proposed fidelity term can describe the complex patterns in residual \mathbf{r} caused by partially known or inaccurate degradation models. Figure 2(d) shows the responses of residual images for a typical filter \mathbf{p}_i , while Figure 2(e) provides the histograms of filter responses. The histograms of filter responses become similar after convolving with the filter \mathbf{p}_i , and can be characterized by the penalty function \mathcal{D}_i . Thus, by setting proper filters $\{\mathbf{p}_i\}_{i=1}^{N_f}$ and penalty functions $\{\mathcal{D}_i\}_{i=1}^{N_f}$, both the spatial dependency and complex distribution of the residual image can be better depicted by the proposed fidelity model. Furthermore, the proposed fidelity model is flexible and applicable to different tasks. With proper training, it can be specified to certain image restoration tasks, such as rain steak removal and image deconvolution with inaccurate blur kernels.

3.2 Regularization Term

To increase modeling capacity on image prior, the regularization term is further parameterized as

$$\mathcal{R}(\mathbf{x}) = \sum_{i=1}^{N} \sum_{j=1}^{N_r} \mathcal{R}_i \left((\mathbf{f}_i \otimes \mathbf{x})_j \right), \tag{10}$$

where \mathbf{f}_i is the *i*-th linear filter, \mathcal{R}_i is the corresponding non-linear penalty function, and N_r is the number of linear filters and penalty functions for the regularization term. The parameters for the regularization term include $\Theta_r = \{\mathbf{f}_i, \mathcal{R}_i\}_{i=1}^{N_r}$. The proposed model is the generalization of the FoE [10] model by parameterizing the regularization term with both the filters and penalty functions. Similar models have also been used in discriminative non-blind image restoration [3], [11].

3.3 SFARL Model

Given a specific image restoration task, the parameters for the fidelity and regularization terms need to be specified. As a large number of parameters are involved in $\mathcal{F}(\mathbf{x})$ and $\mathcal{R}(\mathbf{x})$, it is not feasible to manually determine proper values. In this work, we propose to learn the parameters of both fidelity and regularization terms in a task driven manner.

Denote a training set of S samples by $\{\mathbf{y}_s, \mathbf{x}_s^{gt}\}_{s=1}^S$, where \mathbf{y}_s is the s-th degraded image and \mathbf{x}_s^{gt} is the corresponding ground-truth image. The parameters $\Theta = \{\Theta_f, \Theta_r\}$ can be learned by solving the following bi-level optimization problem,

$$\min_{\Theta} \mathcal{L}(\Theta) = \sum_{s=1}^{S} \ell\left(\mathbf{x}_{s}^{*}, \mathbf{x}_{s}^{gt}\right)$$
s.t.
$$\mathbf{x}_{s}^{*} = \arg\min_{\mathbf{x} \in \mathcal{X}} \sum_{j=1}^{N} \sum_{i=1}^{N_{r}} \mathcal{R}_{i}\left(\left(\mathbf{f}_{i} \otimes \mathbf{x}\right)_{j}\right)$$

$$+\lambda \sum_{j=1}^{N} \sum_{i=1}^{N_{f}} \mathcal{D}_{i}\left(\left(\mathbf{p}_{i} \otimes \left(\mathcal{A}\mathbf{x} - \mathbf{y}_{s}\right)\right)_{j}\right),$$
(11)

where \mathcal{X} is the feasible solution space. For image deconvolution with an inaccurate blur kernel, the feasible solution is only constrained to be in real number space, i.e., $\mathcal{X} = \{\mathbf{x} \mid \mathbf{x} \in \mathbb{R}^N\}$. For rain steak removal, additional constraints on the feasible solution space are required, i.e., $\mathcal{X} = \{\mathbf{x} \mid \forall i, \ 0 \leq x_i \leq y_i\}$, where x_i (and y_i) is the i-th element of clean image \mathbf{x} (and rainy image \mathbf{y}). In principle, the trade-off parameter λ can be absorbed into the non-linear transform \mathcal{D}_i and removed from the model (11). However, the trade-off between the fidelity and regularization terms cannot be easily made due to that the scales of \mathcal{D}_i and \mathcal{R}_i vary for different restoration tasks, thereby making it necessary to include λ in (11).

The loss function $\ell(\cdot)$ measures the dissimilarity between the output of the SFARL model and the ground-truth image. One representative loss used in discriminative image restoration is based on the mean-squared error (MSE) [11],

$$\ell\left(\mathbf{x}, \mathbf{x}^{gt}\right) = \frac{1}{2} \|\mathbf{x} - \mathbf{x}^{gt}\|^2. \tag{12}$$

For image restoration when the precise degradation process is known, the optimal fidelity term in terms of MSE becomes the negative log-likelihood. The standard MAP model $\mathbf{x} = \arg\min_{\mathbf{x}}\frac{\lambda}{2}\|\mathcal{A}\mathbf{x}-\mathbf{y}\|^2+\mathcal{R}(\mathbf{x})$ can then be used in the inner loop of the bi-level optimization task. Thus, the MSE loss is only applicable to learning fidelity term for image restoration with partially known or inaccurate degradation models.

In this work, we use the visual perception metric, e.g., negative SSIM [41], [42], as the loss function,

$$\ell\left(\mathbf{x}, \mathbf{x}^{gt}\right) = -SSIM\left(\mathbf{x}, \mathbf{x}^{gt}\right). \tag{13}$$

The reason of using negative SSIM is two-fold. On one hand, it is known that SSIM is closely related to visual perception of image quality, and minimizing negative SSIM is expected to benefit the visual quality of restoration result. On the other hand, even for image restoration with precise degradation process, the negative log-likelihood will not be the optimal fidelity term when the negative SSIM loss is used. Thus the residual model (9) need to be utilized to learn proper fidelity term from training data for either image deconvolution with inaccurate blur kernels, rain streak removal, or Gaussian denoising. In addition, the experimental results also validate the effectiveness of negative SSIM and residual modeling in terms of both visual quality and perception metric.

4 SFARL TRAINING

In this section, we first present the iterative solution to inner task in the bi-level optimization problem. The SFARL model is then parameterized and gradient-based optimization algorithm can be used for training. Finally, the derivations of gradients for the greedy and end-to-end training processes are presented.

4.1 Iterative Solution to Inner Optimization Task

The inner task in (11) implicitly defines a function $\mathbf{x}^*(\Theta)$ on the model parameters. As the optimization problem is non-convex, it is difficult to obtain the explicit analytic form of either $\mathbf{x}^*(\Theta)$ or $\frac{\partial \mathbf{x}^*(\Theta)}{\partial \Theta}$. In this work, we learn Θ by considering the truncation of an iterative optimization algorithm [3], [11], [12], [33]. Furthermore, the stage-wise model parameters are also used to improve image restoration [3], [11].

To solve (11), the updated solution \mathbf{x}^{t+1} can then be written as a function of \mathbf{x}^t and Θ , i.e., $\mathbf{x}^{t+1}(\Theta;\mathbf{x}^t)$. Suppose that $\{(\Theta^1,\mathbf{x}^1),...,(\Theta^t,\mathbf{x}^t)\}$ are known. The stage-wise parameters Θ^{t+1} can then be learned by solving the following problem,

$$\min_{\Theta^{t+1}} \mathcal{L}(\Theta^{t+1}) = \sum_{s=1}^{S} \ell\left(\mathbf{x}_{s}^{t+1}(\Theta^{t+1}; \mathbf{x}^{t}), \mathbf{x}_{s}^{gt}\right). \tag{14}$$

Here we use a gradient descent method to solve the inner optimization loop, and $\mathbf{x}^{t+1}(\Theta; \mathbf{x}^t)$ can be written as

$$\mathbf{x}^{t+1}(\Theta^{t+1}; \mathbf{x}^{t}) = \mathbf{x}^{t} - \sum_{i=1}^{N_{r}} \mathbf{\bar{f}}_{i}^{t+1} \otimes \phi_{i}^{t+1}(\mathbf{f}_{i}^{t+1} \otimes \mathbf{x}^{t})$$

$$- \lambda^{t+1} \sum_{i=1}^{N_{f}} \mathcal{A}^{\top} \mathbf{\bar{p}}_{i}^{t+1} \otimes \varphi_{i}^{t+1} (\mathbf{p}_{i}^{t+1} \otimes (\mathcal{A}\mathbf{x}^{t} - \mathbf{y})),$$
(15)

where the influence functions are defined as $\varphi_i = \mathcal{D}'_i$ and $\phi_i = \mathcal{R}'_i$. In addition, $\bar{\mathbf{p}}_i$ and $\bar{\mathbf{f}}_i$ are filters by rotating \mathbf{p}_i and \mathbf{f}_i 180 degrees, respectively. After each gradient descent step, \mathbf{x}^{t+1} is projected to the feasible solution space \mathcal{X} .

The gradient-based L-BFGS algorithm [43] is used to solve the optimization problem in (14). Therefore, we need to present the parameterization of the solution in (15) and derive the gradients for the greedy and end-to-end learning processes.

4.2 Parameterization

Similar to [3], [11], we use the weighted summation of Gaussian RBF functions to parameterize the influence functions in regularization term

$$\phi_i(z) = \sum_{j=1}^{M} \pi_{ij} \exp\left(-\frac{\gamma}{2}(z - \mu_j)^2\right),$$
 (16)

and in fidelity term

$$\varphi_i(z) = \sum_{j=1}^{M} w_{ij} \exp\left(-\frac{\gamma}{2}(z - \mu_j)^2\right), \tag{17}$$

where π_{ij} and w_{ij} are weight coefficients, μ_j is mean value and γ is precision.

The filters \mathbf{f}_i in regularization term and \mathbf{p}_i in fidelity term are specified as linear combination of DCT basis with unit norm constraint,

$$\mathbf{f}_i = \mathcal{B}_r \frac{\mathbf{s}_i}{\|\mathbf{s}_i\|_2} \text{ and } \mathbf{p}_i = \mathcal{B} \frac{\mathbf{c}_i}{\|\mathbf{c}_i\|_2},$$
 (18)

where \mathcal{B} is complete DCT basis, \mathcal{B}_r is DCT basis by excluding the DC component, \mathbf{s}_i and \mathbf{c}_i are coefficients for regularization term and fidelity term respectively.

In our implementation, we utilize filters with size 5×5 in both regularization term and fidelity term. We set $N_r=24$ for regularization term, and $N_f=25$ for fidelity term. The numbers of Gaussian functions are fixed to 63 for both fidelity and regularization terms, i.e., M=63. To handle the boundary condition

in convolution operation, the image is padded for processing and only the valid region is cropped for output.

4.3 Greedy Training

The SFARL model is firstly trained stage-by-stage. To learn the model parameters of stage t+1, we need to compute gradient by the chain rule,

$$\frac{\partial \ell(\mathbf{x}^{t+1}, \mathbf{x}^{gt})}{\partial \Theta^{t+1}} = \frac{\partial \mathbf{x}^{t+1}}{\partial \Theta^{t+1}} \frac{\partial \ell(\mathbf{x}^{t+1}, \mathbf{x}^{gt})}{\partial \mathbf{x}^{t+1}}.$$
 (19)

4.3.1 Deviation of $\frac{\partial \ell(\mathbf{x}^{t+1}, \mathbf{x}^{gt})}{\partial \mathbf{x}^{t+1}}$

When the loss function is specified as MSE, i.e., $\ell(\mathbf{x}^{t+1}, \mathbf{x}^{gt}) = \frac{1}{2} \|\mathbf{x}^{t+1} - \mathbf{x}^{gt}\|^2$, the gradient can be simply computed as

$$\frac{\partial \ell(\mathbf{x}^{t+1}, \mathbf{x}^{gt})}{\partial \mathbf{x}^{t+1}} = \mathbf{x}^{t+1} - \mathbf{x}^{gt}.$$
 (20)

Visual perception metric, i.e., negative SSIM

When the loss function is specified as visual perception metric, i.e., $\ell\left(\mathbf{x}^{t+1},\mathbf{x}^{gt}\right) = -\text{SSIM}(\mathbf{x}^{t+1},\mathbf{x}^{gt})$ [41], [42], we give the gradient deviation as follows. To distinct the entire image and small patch, in this subsection we only use \mathbf{X} and \mathbf{Y} as entire image and reference image respectively. The SSIM value is computed based on the small patches \mathbf{x}_i and \mathbf{y}_i

$$SSIM(\mathbf{X}, \mathbf{Y}) = \frac{1}{N_s} \sum_{i=1}^{N_s} ssim(\mathbf{x}_i, \mathbf{y}_i),$$
 (21)

where N_s is the number of patches. The value on each patch is computed as

$$ssim(\mathbf{x}, \mathbf{y}) = \frac{(2\mu_x \mu_y + C_1)(2\sigma_{xy} + C_2)}{(\mu_x^2 + \mu_y^2 + C_1)(\sigma_x^2 + \sigma_y^2 + C_2)},$$
 (22)

where $\mu_x = \frac{1}{N_p} \left(\mathbf{1}^\top \mathbf{x} \right)$ is mean value of patch \mathbf{x} , $\sigma_x^2 = \frac{1}{N_p-1} (\mathbf{x} - \mu_x)^\top (\mathbf{x} - \mu_x)$ is variance of patch \mathbf{x} , and $\sigma_{xy} = \frac{1}{N_p-1} (\mathbf{x} - \mu_x)^\top (\mathbf{y} - \mu_y)$ is covariance of pathes \mathbf{x} and \mathbf{y} , and C_1, C_2 are some constant values. Let us define $A_1 = 2\mu_x\mu_y + C_1$, $A_2 = 2\sigma_{xy} + C_2$, $B_1 = \mu_x^2 + \mu_y^2 + C_1$ and $B_2 = \sigma_x^2 + \sigma_y^2 + C_2$. Then we have $S(\mathbf{x}, \mathbf{y}) = \frac{A_1 A_2}{B_1 B_2}$.

The gradient of negative SSIM is

$$\frac{\partial \left(-\text{SSIM}\left(\mathbf{X}, \mathbf{Y}\right)\right)}{\partial \mathbf{X}} = -\frac{1}{N_s} \sum_{i=1}^{N_s} \frac{\partial \left(\text{ssim}\left(\mathbf{x}_i, \mathbf{y}_i\right)\right)}{\partial \mathbf{Y}}$$

$$= -\frac{1}{N_s} \sum_{i=1}^{N_s} \frac{\partial \left(\text{ssim}\left(\mathbf{x}, \mathbf{y}\right)\right)}{\partial \mathbf{X}} \bigg|_{\mathbf{x} = \mathbf{x}_i, \mathbf{y} = \mathbf{y}_i}, \tag{23}$$

where

$$\begin{split} \frac{\partial \left(\text{ssim} \left(\mathbf{x}, \mathbf{y} \right) \right)}{\partial \mathbf{x}} &= \frac{2}{N_p B_1^2 B_2^2} \left(A_1 B_1 \left(B_2 \mathbf{x} - A_2 \mathbf{y} \right) \right. \\ &+ \left. B_1 B_2 \left(A_2 - A_1 \right) \mu_x \mathbf{1} + A_1 A_2 (B_1 - B_2) \mu_y \mathbf{1} \right). \end{split} \tag{24}$$

For simplicity, we hereafter use **e** to denote $\frac{\partial \ell(\mathbf{x}^{t+1}, \mathbf{x}^{gt})}{\partial \mathbf{x}^{t+1}}$ for both MSE and negative SSIM.

4.3.2 Deviation of $\frac{\partial \mathbf{x}^{t+1}}{\partial \Theta^{t+1}}$

Since the parameterization of fidelity term and regularization term is similar, we only use the fidelity term as an example, and it is easy to extend it to the regularization term.

Weight parameter λ

The gradient with respect to λ is

$$\frac{\partial \mathbf{x}^{t+1}}{\partial \lambda^{t+1}} = -\left(\sum_{i=1}^{N_f} \mathcal{A}^{\top} \bar{\mathbf{p}}_i^{t+1} \otimes \varphi_i^{t+1} \left(\mathbf{p}_i^{t+1} \otimes \left(\mathcal{A} \mathbf{x}^t - \mathbf{y} \right) \right) \right)^{\top}.$$
(25)

The overall gradient with respect to λ is

$$\frac{\partial \ell(\mathbf{x}^{t+1}, \mathbf{x}^{gt})}{\partial \lambda^{t+1}} = -\left(\sum_{i=1}^{N_c} \mathcal{A}^\top \bar{\mathbf{p}}_i^{t+1} \otimes \varphi_i^{t+1} \left(\mathbf{p}_i^{t+1} \otimes \left(\mathcal{A}\mathbf{x}^t - \mathbf{y}\right)\right)\right)^\top \mathbf{e}.$$
(26)

Filter \mathbf{p}_i

The function \mathbf{x}^{t+1} with respect to each filter \mathbf{p}_i can be simplified to.

$$\mathbf{x}^{t+1} = -\lambda^{t+1} \mathcal{A}^{\top} \bar{\mathbf{p}}_i^{t+1} \otimes \varphi_i^{t+1} \left(\mathbf{p}_i^{t+1} \otimes \left(\mathcal{A} \mathbf{x}^t - \mathbf{y} \right) \right) + C,$$
(27)

where C denotes a constant which is independent with \mathbf{p}_i . Let us define $\mathbf{u} = -\mathcal{A}^{\top} \bar{\mathbf{p}}_i^{t+1}$ and $\mathbf{v} = \varphi_i^{t+1} \left(\mathbf{p}_i^{t+1} \otimes (\mathcal{A} \mathbf{x}^t - \mathbf{y}) \right)$. Thus, we can obtain the gradient deviation as

$$\frac{\partial \mathbf{x}^{t+1}}{\partial \mathbf{p}_{i}^{t+1}} = \frac{\partial \mathbf{u}}{\partial \mathbf{p}_{i}^{t+1}} \frac{\partial \mathbf{x}^{t+1}}{\partial \mathbf{u}} + \frac{\partial \mathbf{v}}{\partial \mathbf{p}_{i}^{t+1}} \frac{\partial \mathbf{x}^{t+1}}{\partial \mathbf{v}}.$$
 (28)

Based on the convolution theorem [44], we have

$$\mathbf{u} \otimes \mathbf{v} \Leftrightarrow \mathbf{U}\mathbf{v} \Leftrightarrow \mathbf{V}\mathbf{u},$$
 (29)

where U and V are sparse convolution matrices of u and v, respectively. Thus, the first term in (28) is

$$\frac{\partial \mathbf{u}}{\partial \mathbf{p}^{(t)}} \frac{\partial \mathbf{x}^{(t)}}{\partial \mathbf{u}} = -R_{180}^{\top} \mathcal{A} \mathbf{V}^{\top}, \tag{30}$$

where R_{180} rotates matrix by 180 degrees.

For the second term, we introduce an auxiliary variable $\mathbf{b} = \mathcal{A}\mathbf{x}^t - \mathbf{y}$, $\mathbf{z} = \mathbf{p}_i^{t+1} \otimes \mathbf{b}$, and we have $\mathbf{v} = \varphi_i^{t+1} (\mathbf{z})$. We note that

$$\mathbf{z} = \mathbf{p}_i^{t+1} \otimes \mathbf{b} \Leftrightarrow \mathbf{B} \mathbf{p}_i^{t+1}$$

Therefore, we have

$$\frac{\partial \mathbf{v}}{\partial \mathbf{p}_{i}^{t+1}} \frac{\partial \mathbf{x}^{t+1}}{\partial \mathbf{v}} = \frac{\partial \mathbf{z}}{\partial \mathbf{p}_{i}^{t+1}} \frac{\partial \mathbf{v}}{\partial \mathbf{z}} \frac{\partial \mathbf{x}^{t+1}}{\partial \mathbf{v}} = -\mathbf{B}^{\top} \Lambda \mathbf{U}^{\top}, \quad (31)$$

where $\Lambda=\mathrm{diag}\left(\varphi_i^{t+1'}(z_1),...,\varphi_i^{t+1'}(z_N)\right)$ is a diagonal matrix. The gradient of $\varphi_i(z)$ is

$$\varphi'_{i}(z) = -\gamma \sum_{j=1}^{M} w_{ij} \exp\left(-\frac{\gamma}{2}(z - \mu_{j})^{2}\right) (z - \mu_{j}).$$
 (32)

Since the filter is specified as linear combination of DCT basis, one need to derive the gradient with respect to the combination coefficients \mathbf{c} , i.e.,

$$\frac{\partial \ell}{\partial \mathbf{c}} = \frac{\partial \mathbf{p}}{\partial \mathbf{c}} \frac{\partial \ell}{\partial \mathbf{p}}.$$
 (33)

By introducing $\mathbf{v} = \frac{\mathbf{c}}{\|\mathbf{c}\|_2}$, we then have

$$\frac{\partial \mathbf{p}}{\partial \mathbf{c}} = \frac{\partial \mathbf{v}}{\partial \mathbf{c}} \frac{\partial \mathbf{p}}{\partial \mathbf{v}} = \frac{\partial \mathbf{v}}{\partial \mathbf{c}} \mathcal{B}^{\top}
= \left(\frac{\mathbf{I}}{\|\mathbf{c}\|_{2}} + \frac{\partial (\mathbf{c}^{\top} \mathbf{c})^{-\frac{1}{2}}}{\partial \mathbf{c}} \right) \mathcal{B}^{\top}
= \left(\frac{\mathbf{I}}{\|\mathbf{c}\|_{2}} + \frac{\partial (\mathbf{c}^{\top} \mathbf{c})}{\partial \mathbf{c}} (-\frac{1}{2} \frac{1}{\|\mathbf{c}\|_{2}^{3}}) \mathbf{c}^{\top} \right) \mathcal{B}^{\top}
= \left(\frac{\mathbf{I}}{\|\mathbf{c}\|_{2}} + 2\mathbf{c}(-\frac{1}{2} \frac{1}{\|\mathbf{c}\|_{2}^{3}}) \mathbf{c}^{\top} \right) \mathcal{B}^{\top}
= \frac{1}{\|\mathbf{c}\|_{2}} \left(\mathbf{I} - \frac{\mathbf{c}}{\|\mathbf{c}\|_{2}} \frac{\mathbf{c}^{\top}}{\|\mathbf{c}\|_{2}} \right) \mathcal{B}^{\top}.$$
(34)

Finally, the overall gradient with respect to combination coefficients \mathbf{c}_i^{t+1} is given by

$$\frac{\partial \ell}{\partial \mathbf{c}_i^{t+1}} = -\frac{1}{\|\mathbf{c}_i^{t+1}\|_2} \left(\mathbf{I} - \frac{\mathbf{c}_i^{t+1}}{\|\mathbf{c}_i^{t+1}\|_2} \frac{(\mathbf{c}_i^{t+1})^\top}{\|\mathbf{c}_i^{t+1}\|_2} \right) \mathcal{B}^\top \left(\mathbf{B}^\top \Lambda \mathbf{U}^\top + R_{180}^\top \mathcal{A} \mathbf{V}^\top \right) \mathbf{e}.$$
(35)

Non-linear function φ_i

We first reformulate the function \mathbf{x}^{t+1} with respect to φ_i into the matrix form

$$\mathbf{x}^{t+1} \sim -\lambda^{t+1} \mathcal{A}^{\top} (\mathbf{P}_i^{t+1})^{\top} \varphi_i^{t+1} (\mathbf{b}), \qquad (36)$$

where $\mathbf{b} = \mathbf{P}_i^{t+1} (\mathcal{A} \mathbf{x}^t - \mathbf{y})$. Therefore, the column vector $\varphi_i^{t+1}(\mathbf{b})$ can be reformulated into the matrix form,

$$\varphi_i^{t+1}(\mathbf{b}) = \mathbf{G}(\mathbf{b})\mathbf{w}_i^{t+1},\tag{37}$$

where \mathbf{w}_i is the vectorized version of parameters w_{ij} , matrix $\mathbf{G}(\mathbf{b})$ is

$$\mathbf{G}(\mathbf{b}) = \begin{bmatrix} \exp(-\frac{\gamma}{2}(b_1 - \mu_1)^2) & \exp(-\frac{\gamma}{2}(b_1 - \mu_2)^2) & \cdots & \exp(-\frac{\gamma}{2}(b_1 - \mu_M)^2) \\ \exp(-\frac{\gamma}{2}(b_2 - \mu_1)^2) & \exp(-\frac{\gamma}{2}(b_2 - \mu_2)^2) & \cdots & \exp(-\frac{\gamma}{2}(b_2 - \mu_M)^2) \\ \vdots & \vdots & \ddots & \vdots \\ \exp(-\frac{\gamma}{2}(b_N - \mu_1)^2) & \exp(-\frac{\gamma}{2}(b_N - \mu_2)^2) & \cdots & \exp(-\frac{\gamma}{2}(b_N - \mu_M)^2) \end{bmatrix}$$

Thus, we can get

$$\frac{\partial \mathbf{x}^{t+1}}{\partial \mathbf{w}_{i}^{t+1}} = -\lambda^{t+1} \mathbf{G}^{\mathsf{T}} \mathbf{P}_{i}^{t+1} \mathcal{A}, \tag{38}$$

and finally the overall gradient with respect to \mathbf{w}_i^{t+1} is

$$\frac{\partial \ell}{\partial \mathbf{w}_{i}^{t+1}} = -\lambda^{t+1} \mathbf{G}^{\mathsf{T}} \mathbf{P}_{i}^{t+1} \mathcal{A} \mathbf{e}. \tag{39}$$

In our implementation, we do not explicitly compute the matrix U, V, B, since they can be efficiently operated via 2D convolution.

4.4 End-to-End Training

Once the greedy training process for each stage is carried out, an end-to-end training process is used to fine-tune all the parameters across stages. The joint training loss function is defined as

$$\mathcal{L}(\Theta^1, ..., \Theta^T) = \sum_{s=1}^{S} \ell\left(\mathbf{x}_s^T, \mathbf{x}_s^{gt}\right), \tag{40}$$

where T is the maximum iteration number. The gradient can be computed by the chain rule,

$$\frac{\partial \ell(\mathbf{x}^T, \mathbf{x}^{gt})}{\partial \Theta^t} = \frac{\partial \mathbf{x}^t}{\partial \Theta^t} \frac{\partial \mathbf{x}^{t+1}}{\partial \mathbf{x}^t} \cdots \frac{\partial \ell(\mathbf{x}^T, \mathbf{x}^{gt})}{\partial \mathbf{x}^T}.$$
 (41)

where only $\frac{\partial \mathbf{x}^{t+1}}{\partial \mathbf{x}^t}$ need to be additionally computed. By reformulating the solution in the matrix form,

$$\mathbf{x}^{t+1} = \mathbf{x}^{t} - \sum_{i=1}^{N_r} (\mathbf{F}_i^{t+1})^{\top} \phi_i^{t+1} (\mathbf{F}_i^{t+1} \mathbf{x}^{t})$$

$$-\lambda^{t+1} \sum_{i=1}^{N_f} \mathcal{A}^{\top} (\mathbf{P}_i^{t+1})^{\top} \phi_i^{t+1} (\mathbf{P}_i^{t+1} (\mathcal{A} \mathbf{x}^{t} - \mathbf{y})),$$
(42)

the gradient can be computed as

$$\frac{\partial \mathbf{x}^{t+1}}{\partial \mathbf{x}^t} = \mathbf{I} - \sum_{i=1}^{N_r} (\mathbf{F}_i^{t+1})^\top \Gamma_i \mathbf{F}_i^{t+1} - \sum_{i=1}^{N_f} \mathcal{A}^\top (\mathbf{P}_i^{t+1})^\top \Lambda_i \mathbf{P}_i^{t+1} \mathcal{A},$$
(43)

where $\Gamma_i = \operatorname{diag}\left(\phi_i^{t'}(z_1),...,\phi_i^{t'}(z_N)\right)$ is also a diagonal matrix.

Once $\frac{\partial \mathbf{x}^{t+1}}{\partial \mathbf{x}^t}$ is computed, the overall gradient can be computed by the chain rule and the other gradient parts in (41) can be borrowed from greedy training.

5 EXPERIMENTAL RESULTS

In this section, we evaluate the proposed SFARL algorithm on three restoration tasks, i.e., image deconvolution with an inaccurate blur kernel, rain streak removal from a single image, and Gaussian denoising. For the first two tasks, the SFARL algorithm is compared with the state-of-the-art methods on both synthetic and real images. On the synthetic test datasets, the SFARL models are evaluated in terms of both quantitative metrics and visual quality. In our experiments, the negative SSIM loss is used to train the SFARL model. The filter size in both fidelity and regularization terms is set as 5×5 , and the stage numbers are set as 15, 10 and 5 for image deconvolution, rain streak removal, and Gaussian denoising, respectively. More results and the source code will be made available to the public at https://github.com/csdwren/sfarl.

5.1 Image Deconvolution with Inaccurate Blur Kernels

We consider the blind deconvolution task and use two blur kernel estimation approaches, i.e., Cho and Lee [36] and Xu and Jia [16], for experiments. For each estimation approach, we evaluate the performance of the SFARL model for handling approach-specific blur kernel estimation error. To construct the training dataset, we use eight blur kernels in [46] on 200 clean images from the BSDS dataset [47]. The Gaussian noise with $\sigma=0.25$ is added to generate the blurry images. The methods by Cho and Lee [36] and Xu and Jia [16] are used to estimate blur kernels. Thus, we have 1,600 training samples for each blur kernel estimation approach. To ensure the training sample quality, we randomly select 500 samples with error ratio [46] above 3 for each image deconvolution approach.

TABLE 1: Deblurring results on the dataset by Levin et al. [46] in terms of PSNR.

Kernel estimation	EPLL [2]	ROBUST [13]	SFARL
Cho and Lee [36]	28.83	28.79	29.27
Xu and Jia [16]	29.45	29.37	30.10

Using two synthetic datasets, i.e., Levin et al. [46] and Kohler et al. [45], we compare the SFARL algorithm with the EPLL [2] and ROBUST [13] methods. The dataset by Levin et al. includes 4 clean images and 8 blur kernels. The blur kernels are estimated by Cho and Lee [36] and Xu and Jia [16]. Table 1 and Table

TABLE 2: Deblurring results on the dataset by Levin et al. [46] in terms of SSIM.

Kernel estimation	EPLL [2]	ROBUST [13]	SFARL
Cho and Lee [36]	0.88	0.86	0.89
Xu and Jia [16]	0.90	0.89	0.92

TABLE 3: Deblurring results on the dataset by Kohler et al. in terms of PSNR, and blur kernels are estimated by Xu and Jia [16].

Method	#1	#2	#3	#4	Avg.
EPLL [2]	31.64	26.64	31.45	28.42	29.53
ROBUST [13]	31.49	26.45	31.68	28.30	29.48
SFARL	31.65	26.68	32.24	28.44	29.75

TABLE 4: Deblurring results on the dataset by Kohler et al. in terms of SSIM, and blur kernels are estimated by Xu and Jia [16].

Method	#1	#2	#3	#4	Avg.
EPLL [2]	0.88	0.85	0.91	0.87	0.88
ROBUST [13]	0.87	0.85	0.90	0.86	0.87
SFARL	0.89	0.86	0.92	0.87	0.89

2 show the average PSNR and SSIM values of all evaluated methods on the dataset by Levin et al. [46]. Overall, the SFARL algorithm performs favorably against the other methods in terms of PSNR and SSIM. From Table 1 and Table 2, we also have the following observations. First, the SFARL algorithm models the residual images by specific blur kernel estimation method to improve restoration result. For each blur kernel estimation method, what we need to do is to retrain the SFARL model from the synthetic data. Second, when the estimated blur kernel is more accurate (e.g., Xu and Jia [16]), better quantitative performance indexes are also attained by our SFARL. Third, higher PSNR values can be obtained by our SFARL, albeit it is learned by minimizing the negative SSIM loss.

The dataset by Kohler et al. includes 4 clean images and 12 blur kernels. We use the method by Xu and Jia [16] to estimate blur kernel. Table 3 and Table 4 show that the SFARL algorithm performs favorably against the other methods in terms of PSNR and SSIM. As shown in Figure 3, in terms of visual quality, the EPLL and ROBUST methods generate over-smooth deblurring results. On the other hand, the SFARL algorithm is effective in preserving more detailed texture and suppressing ringing artifacts.

We evaluate the SFARL algorithm against the state-of-the-art methods on two real world blurry images as shown in Figure 4. The blur kernels are estimated using the method by Xu and Jia [16]. As the blur kernel can be accurately estimated in the first image, all the evaluated methods perform well and the SFARL algorithm restores more texture details. On the other hand, the estimated blur kernel is less accurately estimated in the second image. Among all the evaluated methods, the deblurred image by the SFARL algorithm is sharper with fewer ringing effects than those by the other methods. We note that the EPLL method [2] uses the ℓ_2 -norm in the fidelity term, and the ROBUST scheme [13] introduces an ℓ_1 -norm regularizer on the residual **z** caused by kernel error. However, both the ℓ_2 -norm and ℓ_1 -norm are limited to model the complex distribution of the residual. Thus, the performance gain of the SFARL model can be attributed to its effectiveness in characterizing the spatial dependency and complex distribution of residual images.

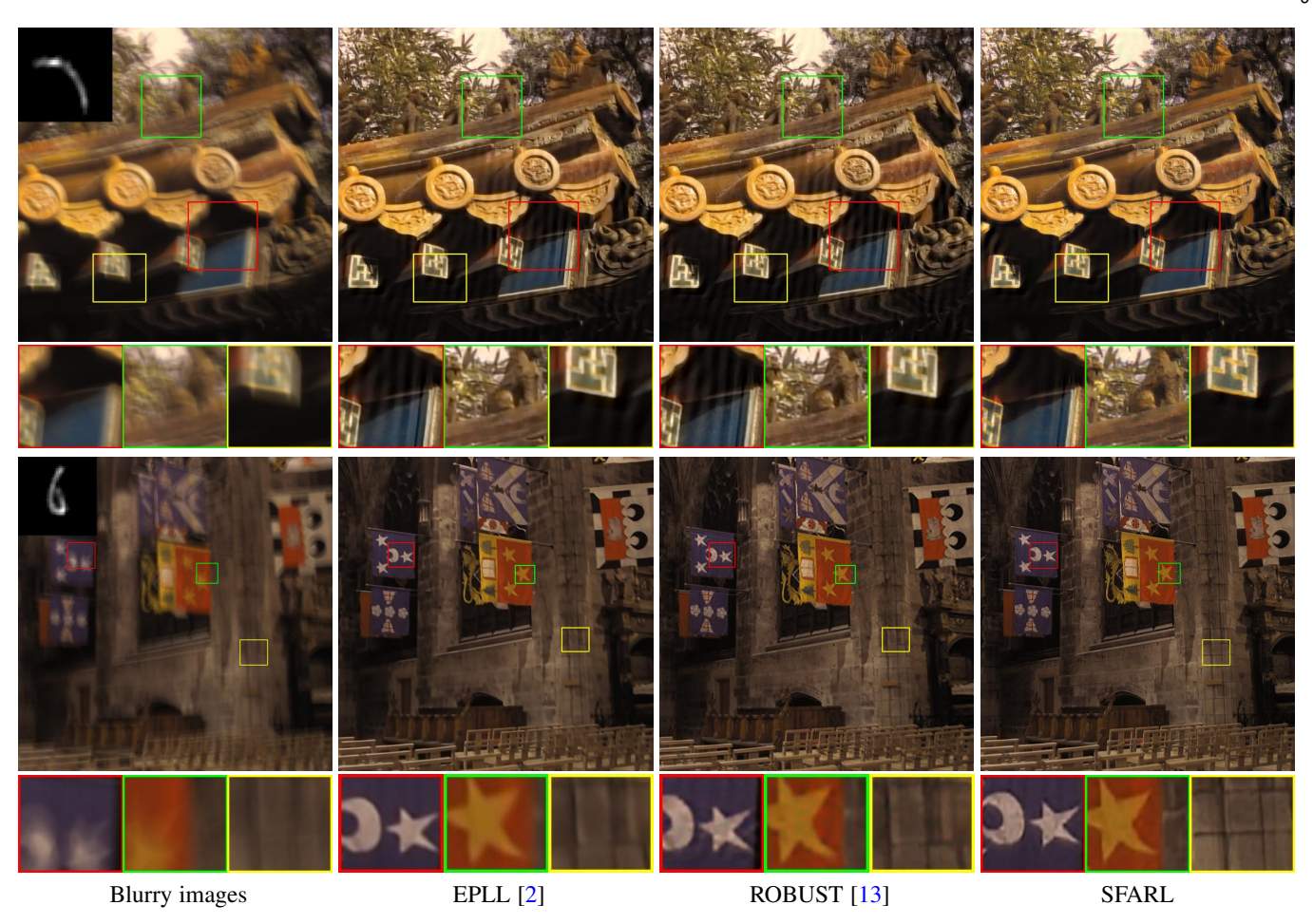


Fig. 3: Deconvolution results on the dataset by Kohler et al. [45] in which blur kernels are estimated by Xu and Jia [16].

5.2 Singe-Image Rain Streak Removal

To train the SFARL model for rain streak removal, we construct a synthetic rainy dataset. We randomly select 100 clean outdoor images from the UCID dataset [48], and use the Photoshop function (http://www.photoshopessentials.com/photo-effects/rain/) to generate 7 rainy images at 7 random rain scales and different orientations ranged from 60 to 90 degrees. The training dataset contains 700 images with different rain orientations and scales, and the sample synthetic rainy images of a clean image are given in Figure 5.

We evaluate the SFARL method with the state-of-the-art algorithms including SR [49], LRA [21], GMM [14], and the CNN [50], on a the synthetic dataset [14]. The dataset consists of 12 rainy images with orientation ranged from left to right. Table 5 and Table 6 show that the SFARL algorithm achieves the highest PSNR and SSIM values for each test image. Figure 6 shows rain steak removal results by all the evaluated algorithms on a synthetic rainy image. The results by the SFARL and GMM algorithms are significantly better than the other methods. However, the result by the GMM method still has visible rain streaks, while the SFARL model recovers satisfying clean image. Figure 7 shows the deraining results of the GMM [14], CNN [50], and SFARL methods on two images in [14]. Overall, the SFARL method removes rain streaks more effectively than the GMM [14] and CNN [50] schemes.

We evaluate the SFARL model on real world rainy images against the state-of-the-art methods. Since the rain in second image

of Figure 8 is too heavy to see rain streaks, we first use the dehazing method [51] before applying a deraining algorithm. On both test images, the SFARL algorithm performs significantly better than the CNN [50] method, and equally well or better than the GMM scheme. For real rainy images, the image formation process is complex and may not be well characterized by either linear additive model nor screen blend model. Nevertheless, due to the flexibility of the fidelity term in modeling spatially dependent and highly complex patterns, the SFARL model is more effective in modeling the complex degradation process and deraining images well.

5.3 Gaussian Denoising

For Gaussian denoising, the SFARL algorithm can also be used to learn proper fidelity term for minimizing negative SSIM loss. To this end, we train three SFARL models for Gaussian denoising with different noise levels, i.e., $\sigma=15,25,50$, respectively. The training dataset consists of 500 images, where 400 are from the BSD dataset [47] and 100 are randomly selected from the UCID dataset [48].

We compare the SFARL model with the state-of-the-art denoising algorithms based on patches, i.e., BM3D [8], EPLL [2] and WNNM [9] approaches, and fields of experts, i.e., CSF [3] and TNRD [11]. Table 7 shows the average SSIM values by different methods on the BSD68 test images. The SFARL algorithm achieves the best average SSIM values at all the noise levels. Note that the SSIM metric is known to be more consistent

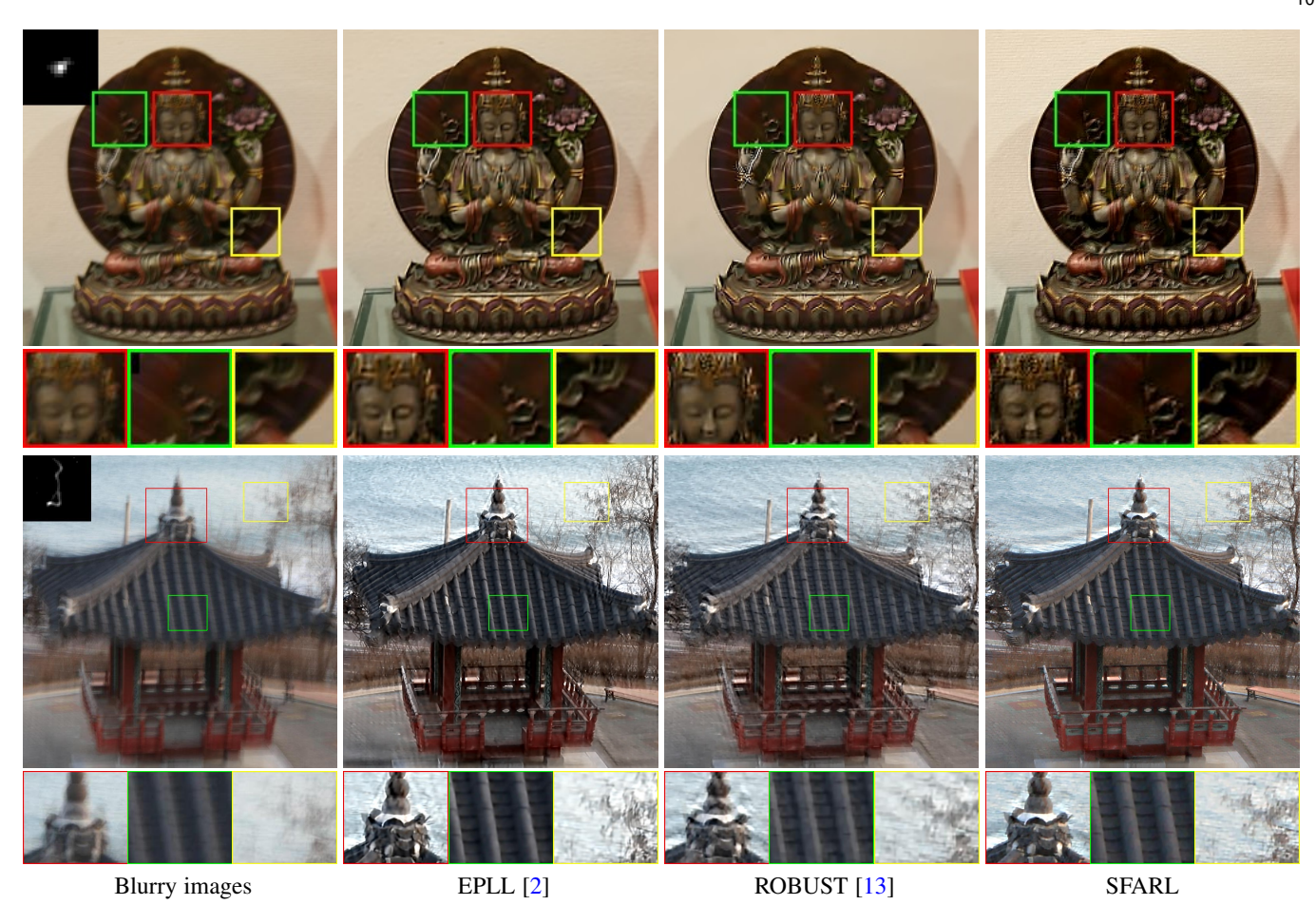


Fig. 4: Deblurring results on real blurry images, in which blur kernels are estimated by Xu and Jia [16].



Fig. 5: Seven synthetic rainy images of a clean outdoor image from the UCID dataset [48].

TABLE 5: Deraining results on the synthetic rainy images in [14] in terms of PSNR.

Method	#1	#2	#3	#4	#5	#6	#7	#8	#9	#10	#11	#12	Avg.
SR [49]	28.57	28.50	25.32	30.08	24.96	25.63	27.47	27.40	27.79	27.42	25.84	27.52	27.21
LRA [21]	30.73	30.38	25.78	36.12	27.94	29.16	33.04	27.65	32.26	28.74	28.92	29.61	30.03
GMM [14]	31.56	33.30	28.05	36.83	29.38	34.88	35.69	30.95	32.73	30.75	29.00	31.20	32.03
CNN [50]	27.58	26.56	23.29	31.02	25.01	25.58	27.82	24.80	27.91	26.83	26.77	26.51	26.64
SFARL	32.91	33.42	28.5	38.45	29.66	34.94	36.40	32.61	35.10	31.87	30.87	32.43	33.09

TABLE 6: Deraining results on synthetic rainy images in [14] in terms of SSIM

Method	#1	#2	#3	#4	#5	#6	#7	#8	#9	#10	#11	#12	Avg.
SR [49]	0.74	0.79	0.84	0.77	0.63	0.73	0.82	0.77	0.74	0.74	0.65	0.77	0.75
LRA [21]	0.83	0.88	0.76	0.96	0.92	0.93	0.94	0.81	0.90	0.82	0.85	0.80	0.87
GMM [14]	0.89	0.93	0.92	0.94	0.90	0.95	0.96	0.90	0.91	0.90	0.86	0.92	0.91
CNN [50]	0.75	0.79	0.71	0.89	0.76	0.80	0.85	0.77	0.81	0.76	0.79	0.73	0.78
SFARL	0.91	0.95	0.92	0.96	0.93	0.97	0.98	0.93	0.94	0.92	0.90	0.93	0.94

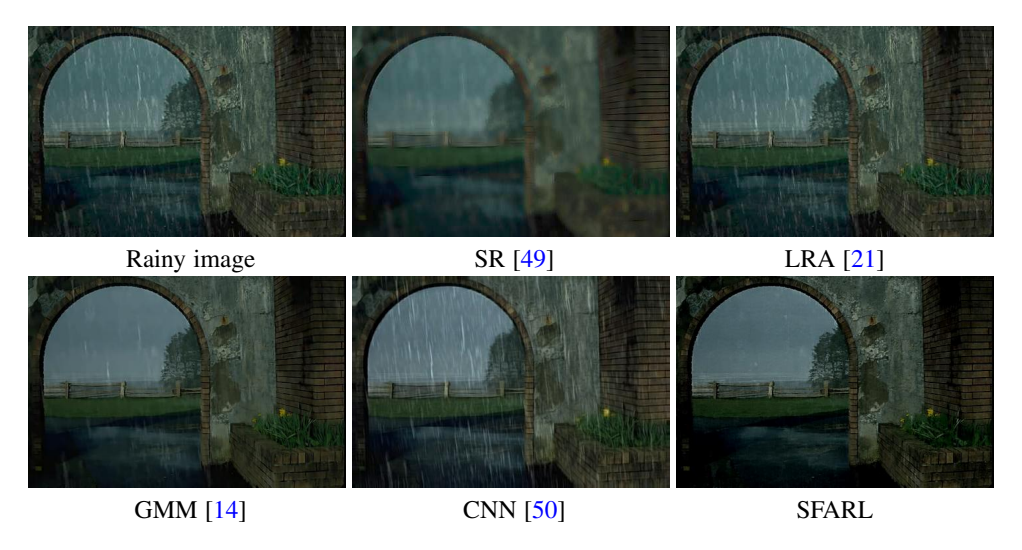


Fig. 6: Rain steak removal results of five evaluated methods on a synthetic image in [14].

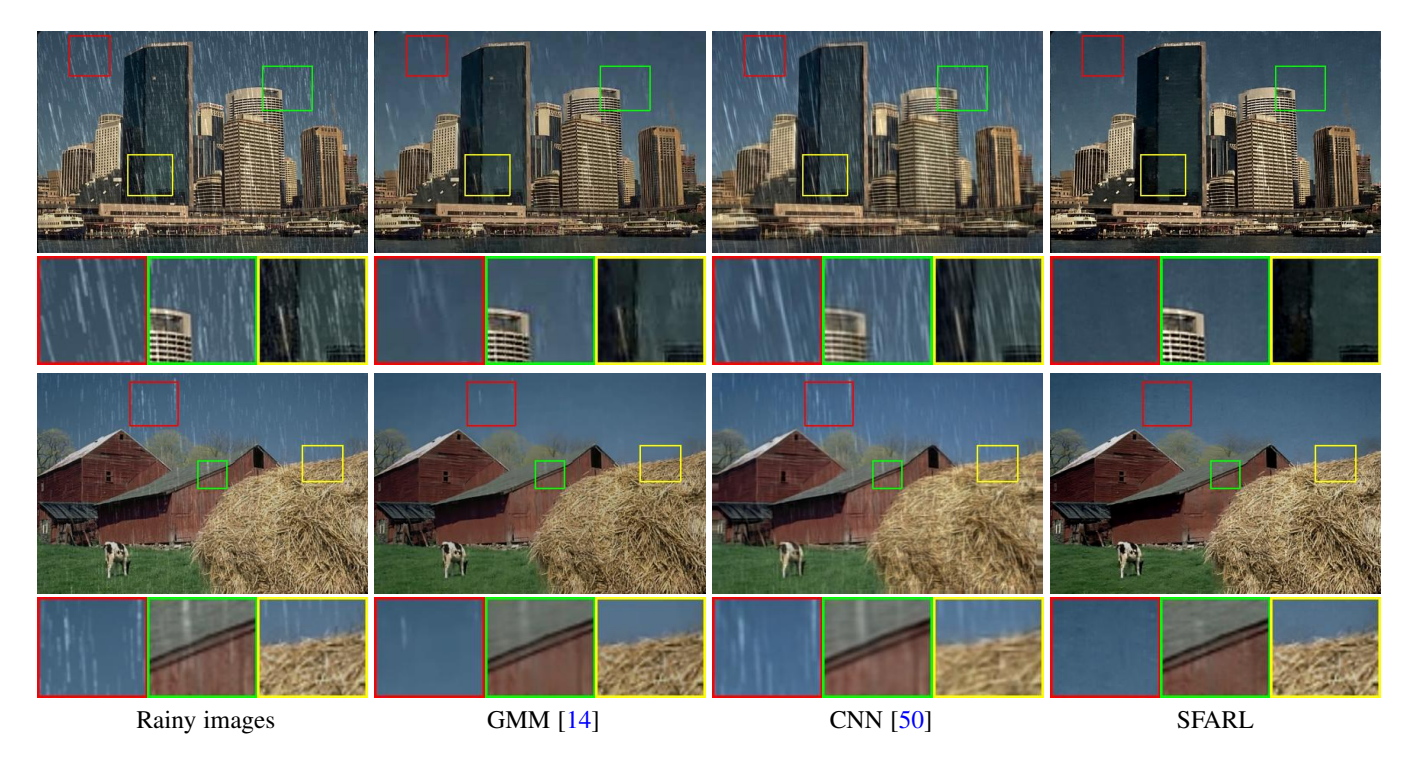


Fig. 7: Results of GMM [14], CNN [50] and SFARL methods on another two synthetic rainy images in [14].

TABLE 7: Gaussian denoising on the BSD68 test images in terms of SSIM.

Noise σ	BM3D [8]	EPLL [2]	WNNM [9]	CSF [3]	TNRD [11]	SFARL
15	0.86	0.87	0.87	0.87	0.87	0.88
25	0.80	0.81	0.81	0.81	0.81	0.82
50	0.69	0.69	0.70	_	0.70	0.71

with human visual perception on image, and the SFARL algorithm performs favorably against the other methods. Figure 9 shows the denoising results with $\sigma=50.$ As shown in the red close-ups, the results by the BM3D and WNNM methods contain visible artifacts, while the results by the SFARL algorithm is visually more pleasant. Compared with the TNRD method, the SFARL model recovers more texture details, indicating that the fidelity term should not be the $\ell_2\text{-norm}$ when the objective is to minimize the negative SSIM loss.

6 CONCLUSIONS

In this paper, we propose an algorithm to effectively handle image restoration with partially known or inaccurate degradation. We present a flexible model to parameterize the fidelity term for characterizing spatial dependency and complex residual distribution of the residual image. The simultaneous fidelity and regularization learning model is developed by incorporating with the parameterized regularization term. With a set of degraded and ground-truth image pairs, task-specific and stage-wise model parameters of

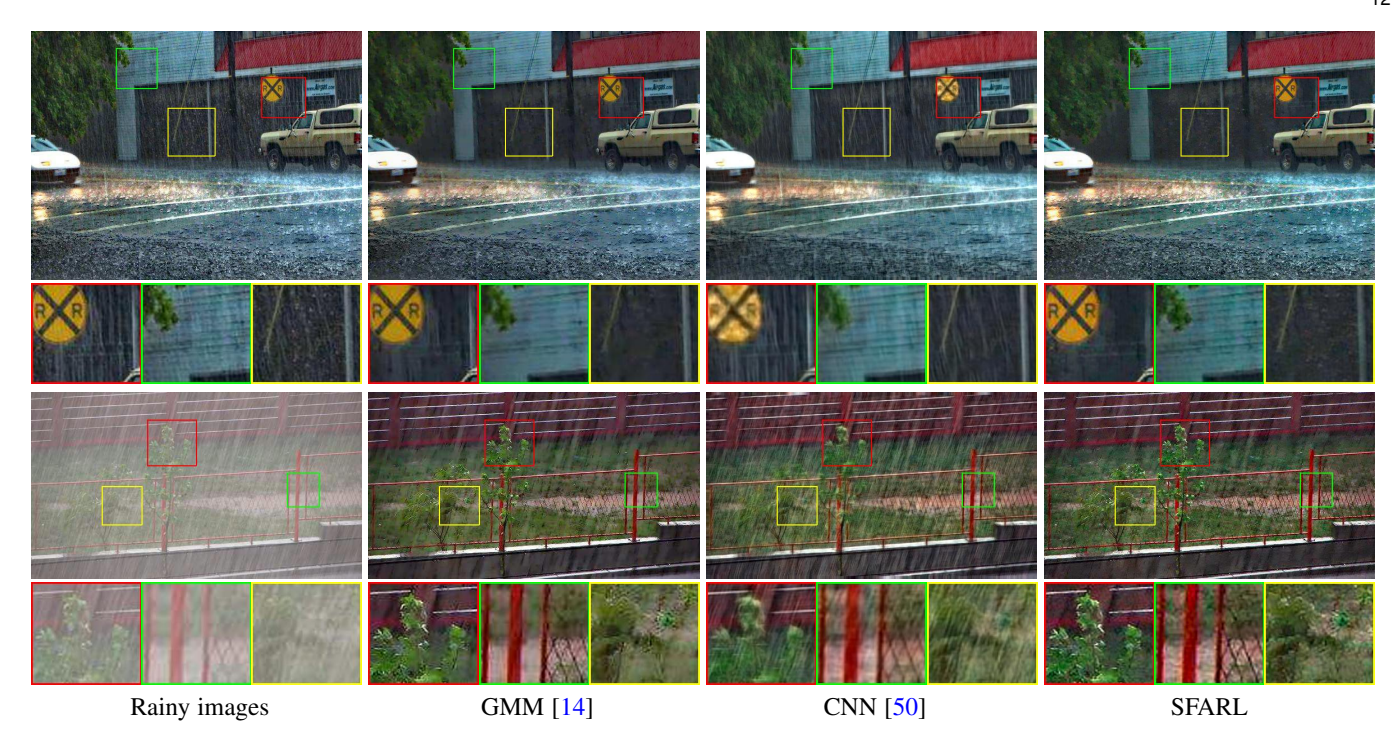


Fig. 8: Results on real rainy images. The rain in second image is very heavy and we first dehaze [51] it to make rain streaks more visible.

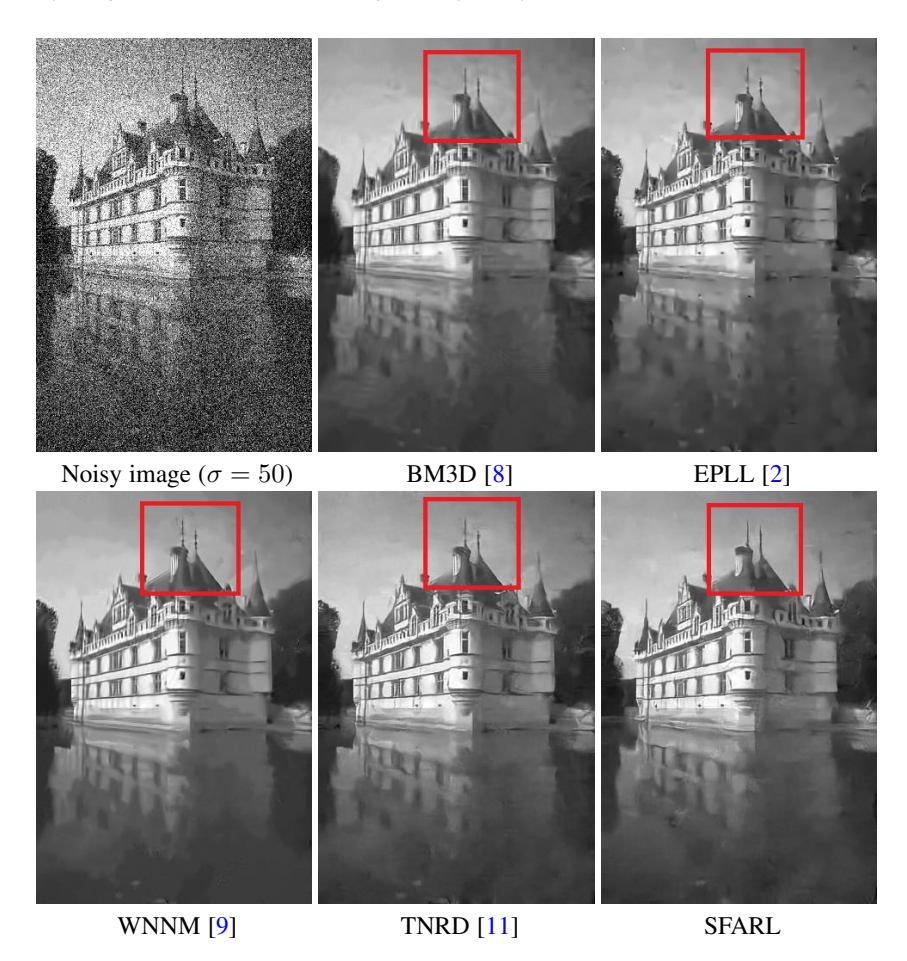


Fig. 9: Gaussian denoising results by all evaluated methods on a test image.

SFARL can then be learned in a task driven manner. Experimental results on two image restoration tasks, i.e., image deconvolution

with inaccurate blur kernels and rain steak removal, show that the SFARL model performs favorably against the state-of-the-

art methods in terms of quantitative metrics and visual quality. Experiments on Gaussian denoising show that the SFARL method is effective in improving visual perception metrics and visual quality of the denoising results. The proposed SFARL algorithm restores images when the degradation process is partially known or inaccurate, and learns proper fidelity term to improve visual perception metric. Our future work includes extending the SFARL model to other restoration tasks, and developing training methods within the unsupervised learning framework.

REFERENCES

- D. Krishnan and R. Fergus, "Fast image deconvolution using hyper-Laplacian priors," in *Advances in Neural Information Processing* Systems, 2009, pp. 1033–1041. 1, 2, 3
- [2] D. Zoran and Y. Weiss, "From learning models of natural image patches to whole image restoration," in *IEEE International Conference on Computer Vision*. IEEE, 2011, pp. 479–486. 1, 2, 3, 8, 9, 10, 11, 12
- [3] U. Schmidt and S. Roth, "Shrinkage fields for effective image restoration," in *Proceedings of the IEEE Conference on Computer Vision and Pattern Recognition*, 2014, pp. 2774–2781. 1, 3, 5, 6, 9, 11
- [4] J. Wright, A. Ganesh, S. Rao, Y. Peng, and Y. Ma, "Robust principal component analysis: Exact recovery of corrupted low-rank matrices via convex optimization," in *Advances in neural information processing* systems, 2009, pp. 2080–2088. 1, 3
- [5] D. Meng and F. De La Torre, "Robust matrix factorization with unknown noise," in *Proceedings of the IEEE International Conference on Com*puter Vision, 2013, pp. 1337–1344. 1, 3
- [6] X. Cao, Y. Chen, Q. Zhao, D. Meng, Y. Wang, D. Wang, and Z. Xu, "Low-rank matrix factorization under general mixture noise distributions," in *Proceedings of the IEEE International Conference on Computer Vision*, 2015, pp. 1493–1501. 1, 3
- [7] A. Chambolle, "An algorithm for total variation minimization and applications," *Journal of Mathematical Imaging and Vision*, vol. 20, no. 1-2, pp. 89–97, 2004.
- [8] K. Dabov, A. Foi, V. Katkovnik, and K. Egiazarian, "Image denoising with block-matching and 3D filtering," in SPIE Electronic Imaging, 2006. 1, 2, 9, 11, 12
- [9] S. Gu, L. Zhang, W. Zuo, and X. Feng, "Weighted nuclear norm minimization with application to image denoising," in *Proceedings of the IEEE Conference on Computer Vision and Pattern Recognition*, 2014, pp. 2862–2869. 1, 9, 11, 12
- [10] S. Roth and M. J. Black, "Fields of experts," *International Journal of Computer Vision*, vol. 82, no. 2, pp. 205–229, 2009. 1, 3, 5
- [11] Y. Chen, W. Yu, and T. Pock, "On learning optimized reaction diffusion processes for effective image restoration," in *Proceedings of the IEEE Conference on Computer Vision and Pattern Recognition*, 2015, pp. 5261–5269. 1, 3, 5, 6, 9, 11, 12
- [12] Y. Chen and T. Pock, "Trainable nonlinear reaction diffusion: A flexible framework for fast and effective image restoration," *IEEE Transactions* on Pattern Analysis and Machine Intelligence, vol. 39, no. 6, pp. 1256– 1272, 2017. 1, 3, 6
- [13] H. Ji and K. Wang, "Robust image deblurring with an inaccurate blur kernel," *IEEE Transactions on Image Processing*, vol. 21, no. 4, pp. 1624–1634, 2012. 2, 3, 4, 8, 9, 10
- [14] Y. Li, R. T. Tan, X. Guo, J. Lu, and M. S. Brown, "Rain streak removal using layer priors," in *Proceedings of the IEEE Conference on Computer Vision and Pattern Recognition*, 2016, pp. 2736–2744. 2, 4, 9, 10, 11, 12
- [15] A. Goldstein and R. Fattal, "Blur-kernel estimation from spectral irregularities," in *European Conference on Computer Vision*. Springer, 2012, pp. 622–635.
- [16] L. Xu and J. Jia, "Two-phase kernel estimation for robust motion deblurring," in *European Conference on Computer Vision*. Springer, 2010, pp. 157–170. 2, 3, 4, 8, 9, 10
- [17] W. Zuo, D. Ren, D. Zhang, S. Gu, and L. Zhang, "Learning iteration-wise generalized shrinkage-thresholding operators for blind deconvolution," *IEEE Transactions on Image Processing*, vol. 25, no. 4, pp. 1751–1764, 2016. 2, 3
- [18] W. Ren, X. Cao, J. Pan, X. Guo, W. Zuo, and M.-H. Yang, "Image deblurring via enhanced low-rank prior," *IEEE Transactions on Image Processing*, vol. 25, no. 7, pp. 3426–3437, 2016. 2
- [19] J. Pan, D. Sun, H. Pfister, and M.-H. Yang, "Blind image deblurring using dark channel prior," in *Proceedings of the IEEE Conference on Computer Vision and Pattern Recognition*, 2016, pp. 1628–1636.

- [20] J. Pan, Z. Hu, Z. Su, and M.-H. Yang, "l₀-regularized intensity and gradient prior for deblurring text images and beyond," *IEEE Transactions* on Pattern Analysis and Machine Intelligence, vol. 39, no. 2, pp. 342– 355, 2017. 2, 3
- [21] Y.-L. Chen and C.-T. Hsu, "A generalized low-rank appearance model for spatio-temporally correlated rain streaks," in *Proceedings of the IEEE International Conference on Computer Vision*, 2013, pp. 1968–1975. 2, 4, 9, 10, 11
- [22] Y. Luo, Y. Xu, and H. Ji, "Removing rain from a single image via discriminative sparse coding," in *Proceedings of the IEEE International* Conference on Computer Vision, 2015, pp. 3397–3405. 2, 4
- [23] A. Eriksson and A. Van Den Hengel, "Efficient computation of robust low-rank matrix approximations in the presence of missing data using the 1 1 norm," in *Proceedings of the IEEE Conference on Computer* Vision and Pattern Recognition. IEEE, 2010, pp. 771–778. 3
- [24] Q. Zhao, D. Meng, Z. Xu, W. Zuo, and L. Zhang, "Robust principle component analysis with complex noise," in *International Conference on Machine Learning*, 2014, pp. 55–63.
- [25] X. Chen, Z. Han, Y. Wang, Q. Zhao, D. Meng, and Y. Tang, "Robust tensor factorization with unknown noise," in *Proceedings of the IEEE Conference on Computer Vision and Pattern Recognition*, 2016, pp. 5213–5221.
- [26] P. Chen, N. Wang, N. L. Zhang, and D.-Y. Yeung, "Bayesian adaptive matrix factorization with automatic model selection," in *Proceedings of* the IEEE Conference on Computer Vision and Pattern Recognition, 2015, pp. 1284–1292. 3
- [27] Z. Gong, Z. Shen, and K.-C. Toh, "Image restoration with mixed or unknown noises," *Multiscale Modeling & Simulation*, vol. 12, no. 2, pp. 458–487, 2014. 3
- [28] F. Zhu, G. Chen, and P.-A. Heng, "From noise modeling to blind image denoising," in *Proceedings of the IEEE Conference on Computer Vision* and Pattern Recognition, 2016, pp. 420–429. 3
- [29] J. Xu, D. Ren, L. Zhang, and D. Zhang, "Patch group based Bayesian learning for blind image denoising," in *Asian Conference on Computer Vision*. Springer, 2016, pp. 79–95. 3
- [30] M. Aharon, M. Elad, and A. Bruckstein, "K-SVD: An algorithm for designing overcomplete dictionaries for sparse representation," *IEEE Transactions on Signal Processing*, vol. 54, no. 11, pp. 4311–4322, 2006.
- [31] U. Schmidt, C. Rother, S. Nowozin, J. Jancsary, and S. Roth, "Discriminative non-blind deblurring," in *Proceedings of the IEEE Conference on Computer Vision and Pattern Recognition*, 2013, pp. 604–611.
- [32] U. Schmidt, J. Jancsary, S. Nowozin, S. Roth, and C. Rother, "Cascades of regression tree fields for image restoration," *IEEE Transactions on Pattern Analysis and Machine Intelligence*, vol. 38, no. 4, pp. 677–689, 2016. 3
- [33] L. Xiao, J. Wang, W. Heidrich, and M. Hirsch, "Learning high-order filters for efficient blind deconvolution of document photographs," in *European Conference on Computer Vision*. Springer, 2016, pp. 734– 749, 3, 6
- [34] S. Ryan Fanello, C. Keskin, P. Kohli, S. Izadi, J. Shotton, A. Criminisi, U. Pattacini, and T. Paek, "Filter forests for learning data-dependent convolutional kernels," in *Proceedings of the IEEE Conference on Computer* Vision and Pattern Recognition, 2014, pp. 1709–1716. 3
- [35] K. Zhang, W. Zuo, S. Gu, and L. Zhang, "Learning deep CNN denoiser prior for image restoration," *Proceedings of the IEEE Conference on Computer Vision and Pattern Recognition*, 2017.
- [36] S. Cho and S. Lee, "Fast motion deblurring," ACM Transactions on Graphics, vol. 28, no. 5, p. 145, 2009. 3, 8
- [37] Q. Shan, J. Jia, and A. Agarwala, "High-quality motion deblurring from a single image," in *ACM Transactions on Graphics (TOG)*, vol. 27, no. 3, 2008, p. 73. 3
- [38] D. Perrone, A. Ravichandran, R. Vidal, and P. Favaro, "Image priors for image deblurring with uncertain blur." in *The British Machine Vision Conference (BMVC)*, 2012, pp. 1–11.
- [39] L. Yuan, J. Sun, L. Quan, and H.-Y. Shum, "Progressive inter-scale and intra-scale non-blind image deconvolution," in ACM Transactions on Graphics (TOG), vol. 27, no. 3, 2008, p. 74. 3
- [40] F. Heide, M. Rouf, M. B. Hullin, B. Labitzke, W. Heidrich, and A. Kolb, "High-quality computational imaging through simple lenses," ACM Transactions on Graphics (TOG), vol. 32, no. 5, p. 149, 2013. 3
- [41] Z. Wang, A. C. Bovik, H. R. Sheikh, and E. P. Simoncelli, "Image quality assessment: from error visibility to structural similarity," *IEEE Transactions on Image Processing*, vol. 13, no. 4, pp. 600–612, 2004. 5, 6

- [42] Z. Wang and Q. Li, "Information content weighting for perceptual image quality assessment," *IEEE Transactions on Image Processing*, vol. 20, no. 5, pp. 1185–1198, 2011. 5, 6
- [43] M. Schmidt, "minFunc: unconstrained differentiable multivariate optimization in matlab," http://www.cs.ubc.ca/~schmidtm/Software/ minFunc.html, 2005. 6
- [44] R. N. Bracewell and R. N. Bracewell, The Fourier Transform and Its Applications. McGraw-Hill, New York, 1986. 7
- [45] R. Köhler, M. Hirsch, B. Mohler, B. Schölkopf, and S. Harmeling, "Recording and playback of camera shake: Benchmarking blind deconvolution with a real-world database," in *European Conference on Computer Vision*. Springer, 2012, pp. 27–40. 8, 9
- [46] A. Levin, Y. Weiss, F. Durand, and W. T. Freeman, "Understanding and evaluating blind deconvolution algorithms," in *Proceedings of the IEEE Conference on Computer Vision and Pattern Recognition*. IEEE, 2009, pp. 1964–1971. 8
- [47] D. Martin, C. Fowlkes, D. Tal, and J. Malik, "A database of human segmented natural images and its application to evaluating segmentation algorithms and measuring ecological statistics," in *Proceedings of the IEEE International Conference on Computer Vision*, vol. 2. IEEE, 2001, pp. 416–423. 8, 9
- [48] G. Schaefer and M. Stich, "UCID: An uncompressed color image database," in *Electronic Imaging*. International Society for Optics and Photonics, 2003, pp. 472–480. 9, 10
- [49] L.-W. Kang, C.-W. Lin, and Y.-H. Fu, "Automatic single-image-based rain streaks removal via image decomposition," *IEEE Transactions on Image Processing*, vol. 21, no. 4, pp. 1742–1755, 2012. 9, 10, 11
- [50] D. Eigen, D. Krishnan, and R. Fergus, "Restoring an image taken through a window covered with dirt or rain," in *Proceedings of the IEEE International Conference on Computer Vision*, 2013, pp. 633–640. 9, 10, 11, 12
- [51] G. Meng, Y. Wang, J. Duan, S. Xiang, and C. Pan, "Efficient image dehazing with boundary constraint and contextual regularization," in Proceedings of the IEEE International Conference on Computer Vision, 2013, pp. 617–624. 9, 12



David Zhang graduated in Computer Science from Peking University. He received his MSc in 1982 and his PhD in 1985 in Computer Science from the Harbin Institute of Technology (HIT), respectively. From 1986 to 1988 he was a Post-doctoral Fellow at Tsinghua University and then an Associate Professor at the Academia Sinica, Beijing. In 1994 he received his second PhD in Electrical and Computer Engineering from the University of Waterloo, Ontario, Canada. He is a Chair Professor since 2005 at the Hong Kong

Polytechnic University where he is the Founding Director of the Biometrics Research Centre (UGC/CRC) supported by the Hong Kong SAR Government in 1998. He also serves as Visiting Chair Professor in Tsinghua University, and Adjunct Professor in Peking University, Shanghai Jiao Tong University, HIT, and the University of Waterloo. He is Founder and Editor-in-Chief, International Journal of Image and Graphics (IJIG); Founder and Series Editor, Springer International Series on Biometrics (KISB); Organizer, International Conference on Biometrics Authentication (ICBA); Associate Editor of more than ten international journals including IEEE Transactions and so on. So far, he has published about 20 monographs, over 400 international journal papers and around 40 patents from USA/Japan/HK/China. He was selected as a Highly Cited Researcher in Engineering by Thomson Reuters in 2014, 2015 and 2016, respectively. Professor Zhang is a Croucher Senior Research Fellow, Distinguished Speaker of the IEEE Computer Society, and a Fellow of both IEEE and IAPR.



Dongwei Ren received the B.Sc. degree in bioinfomatics and the M.Sc. degree in computer science and technology from the Harbin Institute of Technology, Harbin, China, in 2011 and 2013, respectively. He is currently working under the joint Ph.D. programmes in the School of Computer Science and Technology, Harbin Institute of Technology, and the Department of Computing, The Hong Kong Polytechnic University. From November 2012 to January 2013 and from April 2014 to August 2014, he was a Research Assis-

tant at the Department of Computing, The Hong Kong Polytechnic University. His research interests include low level vision and discriminative learning.



Lei Zhang is a Chair Professor in the Department of Computing, The Hong Kong Polytechnic University. His research interests include Computer Vision, Pattern Recognition, Image and Video Analysis, and Biometrics, etc. Prof. Zhang has published more than 200 papers in those areas. As of 2017, his publications have been cited more than 26,000 times in the literature. Prof. Zhang is an Associate Editor of IEEE Trans. on Image Processing, SIAM Journal of Imaging Sciences and Image and Vision Computing, etc.

He is a Web of Science Highly Cited Researcher selected by Thomson Reuters.



Wangmeng Zuo received the Ph.D. degree in computer application technology from the Harbin Institute of Technology, Harbin, China, in 2007. He is currently a Professor in the School of Computer Science and Technology, Harbin Institute of Technology. His current research interests include image enhancement and restoration, object detection, visual tracking, and image classification. He has published over 70 papers in toptier academic journals and conferences. He has served as a Tutorial Organizer in ECCV 2016,

an Associate Editor of the *IET Biometrics* and *Journal of Electronic Imaging*, and the Guest Editor of *Neurocomputing*, *Pattern Recognition*, *IEEE Transactions on Circuits and Systems for Video Technology*, and *IEEE Transactions on Neural Networks and Learning Systems*.



Ming-Hsuan Yang is a Professor in Electrical Engineering and Computer Science at University of California, Merced. He received his PhD degree in computer science from the University of Illinois at Urbana-Champaign in 2000. Yang served as an associate editor of the IEEE Transactions on Pattern Analysis and Machine Intelligence from 2007 to 2011, and is an associate editor of the International Journal of Computer Vision, Image and Vision Computing, and Journal of Artificial Intelligence Research. He

received the Google Faculty Award in 2009 and the NSF CAREER Award in 2012. He is a senior member of the IEEE and the ACM.